ORNL/TM-2017/438

Light Water Reactor Sustainability Program

Development of Computational Tools for Modeling Thermal and Radiation Effects on Grain Boundary Segregation and Precipitation in Fe-Cr-Ni-based Alloys

August 2017

U.S. Department of Energy

Office of Nuclear Energy

ORNL/TM-2017/438

Development of Computational Tools for Modeling Thermal and Radiation effects on Grain Boundary Segregation and Precipitation in Fe-Cr-Ni-based Alloys

Ying Yang

08/2017

Prepared for the
U.S. Department of Energy
Office of Nuclear Energy

ABSTRACT

This work aims at developing computational tools for modeling thermal and radiation effects on solute segregation at grain boundaries (GBs) and precipitation. This report described two major efforts. One is the development of computational tools on integrated modeling of thermal equilibrium segregation (TES) and radiation-induced segregation (RIS), from which synergistic effects of thermal and radiation, and pre-existing GB segregation have been taken into consideration. This integrated modeling was used in describing the Cr and Ni segregation in the Fe-Cr-Ni alloys. The other effort is thermodynamic modeling on the Fe-Cr-Ni-Mo system which includes the major alloying elements in the investigated alloys in the Advanced Radiation Resistant Materials (ARRM) program. Through thermodynamic calculation, we provide baseline thermodynamic stability of the hardening phase $Ni_2(Cr,Mo)$ in selected Ni-based super alloys, and contribute knowledge on mechanistic understanding on the formation of $Ni_2(Cr,Mo)$ in the irradiated materials. The major outcomes from this work are listed in the following:

1) Under the simultaneous thermal and irradiation conditions, radiation-induced segregation played a dominant role in the GB segregation. The pre-existing GB segregation only affects the subsequent radiation-induced segregation in the short time. For the same element, the segregation tendency of Cr and Ni due to TES is opposite to that from RIS. The opposite tendency can lead to the formation of W-shape profile. These findings are consistent with literature observation of the transitory W-shape profile.
2) While TES only affects the distance of one or two atomic layers from GBs, the RIS can affect a broader distance from GB. Therefore, the W-shape due to pre-existing GB segregation is much narrower than that due to composition gradient formed during the transient state. Considering the measurement resolution of Auger or STEM analysis, the segregation tendency due to RIS should play a dominant role in the measured values. However, The GB segregation due to pre-existing GB segregation may affect the chemical potential of element at GB, and subsequently the corrosion resistance.
3) Based on the newly developed thermodynamic database of Fe-Cr-Ni-Mo, we predicted the $Ni_2(Cr,Mo)$ as a thermodynamically stable phase in all investigated low Fe-content Ni-based alloys. The calculated phase amount decreases with the increasing Fe content, being consistent with that observed in the irradiated materials.
4) The formation of the $Ni_2(Cr,Mo)$ phase in irradiated materials is due to irradiation enhanced diffusion. The calculated equilibrium $Ni_2(Cr,Mo)$ amount is more than that observed in the irradiated materials, suggesting that the amount of $Ni_2(Cr,Mo)$ is likely to increase more with further irradiation.

ACKNOWLEDGEMENTS

This work was supported by the U.S. Department of Energy (DOE), Office of Nuclear Energy, Light Water Reactor Sustainability (LWRS) Research and Development Effort, under contract DE-AC05-00OR22725 with UT-Battelle, LLC. Discussions with Drs. J.T. Busby, and K. Leonard at ORNL and Dr. Miao Song at University of Michigan are acknowledged.

CONTENTS

FIGURES

ACRONYMS

SS: Stainless Steels

RIS: Radiation Induced Segregation

TES: Thermal Equilibrium Segregation

GB: Grain Boundary

IASCC: Irradiation Induced Stress Corrosion Cracking

LWRs: Light Water Reactors sustainability

CT: Computational Thermodynamics

CALPHAD: CALculation of PHAse Diagram

FCC: Face Center Cubic

CTE: Coefficient of Thermal Expansion

1. Introduction

Austenitic stainless steels (SS) are widely used in light water reactors (LWRs). However, the combined long-term neutron irradiation and thermal conditions impose great challenges on the stability of materials. For example, a variety of microstructural and microchemical changes have been reported in austenitic SS core internals of LWRs, primarily including a high density (10^{22}–10^{23} m^3) of Frank loops (< approximately 20 nm), precipitates (e.g., Ni/Si-rich γ', G-phases and carbides), and cavities, as well as chemical segregation at grain boundaries (GBs) and dislocations [1-5]. These changes lead to material degradation such as irradiation-assisted stress corrosion cracking (IASCC). IASCC has been linked to the depletion of Cr at the grain boundary as a result of radiation-induced segregation (RIS) [2]. RIS modeling of Fe-Cr-Ni system has been subjected to several prior studies [6-13]. Recently, Yang et al. [14] has developed an improved RIS model based on Perks model [15] by integrating computational thermodynamics (CT) [16] into the modeling of compositional dependent diffusion coefficients and thermodynamic factors, and interstitial binding model [13] into the modeling diffusion flux of interstitials. One of the major findings is that the elemental segregation in the steady state is the result of not only preferential coupling of elements with defects but also the composition gradient in the vicinity of the grain boundary that was formed during the transient state. The composition gradient during the transient state can contribute to the oscillatory behavior of segregation profile in the GBs. While the previous study shows the composition gradient that formed from the transient state has an important role in the steady-state microchemistry at defect sinks, Busby et al. [17] found that the pre-existing Cr-enrichment at grain boundary due to thermal segregation also leads to the non-monotonic behavior of segregation profiles during the subsequent irradiation. Similarly, Cole et al. [18] found Cr, Mo and P in 316SS under different cooling rates had already enriched to various levels at grain boundary before the materials being exposed to irradiation environments. The higher the enriched levels lead to the more pronounced W-shape profile during the subsequent irradiation. Nastar et al. [19] did a mean-field RIS kinetics simulation and also found a W-shape profile of Cr when using a pre-enriched Cr profile as input. It becomes evident that pre-enrichment of element at GBs due to thermal segregation also plays a role in the subsequent RIS profile as well as the microchemistry at GBs [17-19].

Austenitic stainless steels suffer from serious irradiation-assisted stress corrosion cracking (IASCC) in Light Water Reactor (LWR) environments. Under the Advanced Radiation Resistant Materials (ARRM) program [20], which is aimed at identifying promising candidates to replace Austenitic stainless steels, several Ni-based superalloys 625, 625Plus, 625DA, 725, X750, 718A, 690, and C22 have been investigated to explore radiation effect on hardening and stress corrosion cracking. After 5dpa proton irradiation, long range order phase $Ni_2(Cr,Mo)$ was observed in alloy 625, 625plus, 625DA, 725, and 690. This long range ordered phase was not observed in these alloys before irradiation. The amount of the $Ni_2(Cr,Mo)$ phase in the irradiated samples was found to be directly relevant to the irradiation hardening. For example, the hardness of the C22 alloy with the highest amount of $Ni_2(Cr,Mo)$ phase increased ~150% after irradiation, while for the 718 alloy, there was almost no irradiation hardening as no $Ni_2(Cr,Mo)$ was formed after irradiation.

This work aims at developing computational tools for modeling thermal and radiation effects on solute segregation at grain boundaries and precipitation. This report described two major efforts. One is the development of computational tools on integrated modeling of thermal equilibrium segregation (TES) and radiation-induced segregation (RIS), from which synergistic effects of

thermal and radiation, pre-existing GB segregation have been taken into consideration. The other effort is thermodynamic modeling on the Fe-Cr-Ni-Mo system which includes the major alloying elements in the investigated alloys in the ARRM program. Through thermodynamic calculation, we provide baseline thermodynamic stability of the hardening phase Ni_2(Cr,Mo) in selected Ni-based super alloys, and contribute knowledge on mechanistic understanding on the formation of Ni_2(Cr,Mo) in the irradiated materials.

2. Thermodynamic and kinetic modeling of thermal equilibrium GB segregation in Fe-Cr-Ni alloys

2.1 Thermodynamic model

Thermodynamic modeling of equilibrium segregation is based on the **Langmuir-McLean segregation** approach [21-23]. Several ways have been used to derive the segregation isotherms based on this approach. The method used by duPlessis and van Wyk [24] is briefly discussed here. Consider a closed system containing the GB inside the crystalline surrounding. The GB is considered as a region of finite thickness, while the bulk of the crystal is of infinite size. GB segregation is then defined as a redistribution of solute atoms between the crystal and the interface. From this point of view, both parts of the system are considered as open, enabling an exchange of solutes. Using Cr as an example, the basic condition for chemical equilibrium between the solute Cr and solvent Fe at the grain boundary φ and the bulk *B* is $Fe^B + Cr^\varphi = Fe^\varphi + Cr^B$. The Gibbs energy of reaction at equilibrium is

$$\Delta G = \left(\mu_{Cr}^{\varphi} - \mu_{Cr}^{B}\right) - \left(\mu_{Fe}^{\varphi} - \mu_{Fe}^{B}\right) = 0 \,, \tag{1}$$

where μ_s^l represents the chemical potential of the *s* element in the *l* state, *s* represents element Cr or Fe, and *l* represents phase φ or *B*. Because

$$\mu_s^l = \mu_s^{l,0} + RTln(a_s^l) \,, \tag{2}$$

$\mu_s^{l,0}$ is the standard chemical potential of the *s* element in the *l* state, and a_s^l denotes the activity coefficient of *s* in *l*. Combining Eqs. (1) and (2), we obtain

$$\frac{a_{Cr}^{\varphi}}{a_{Fe}^{\varphi}} = \frac{a_{Cr}^{B}}{a_{Fe}^{B}} \exp\left(-\frac{\Delta G_{Cr}^{0}}{RT}\right) \,, \tag{3}$$

where a_{Cr}^{φ}denotes the activity of Cr in φ, a_{Fe}^{φ}, a_{Cr}^{B} and a_{Fe}^{B} were similarly defined, and ΔG_{Cr}^{0} is the standard molar Gibbs energy of segregation, as described by Eq. (4). It is a composition-independent quantity.

$$\Delta G_{Cr}^{0} = (\mu_{Fe}^{B,0} - \mu_{Cr}^{B,0}) - (\mu_{Fe}^{\varphi,0} - \mu_{Cr}^{\varphi,0}) \,. \tag{4}$$

Because $a_s^l = \gamma_s^l x_s^l$, with γ_s^l as the activity coefficient and x_s^l the atomic concentration of *s* in *l*, Eq. (3) can be written as

$$\frac{x_{Cr}^{\varphi}}{1-x_{Cr}^{\varphi}} = \frac{x_{Cr}^{B}}{1-x_{Cr}^{B}} \exp\left(-\frac{(\Delta G_{Cr}^{0}+\Delta G_{Cr}^{E})}{RT}\right) , \tag{5}$$

where ΔG_{Cr}^{E} is the excess molar Gibbs energy of segregation, which equals to

$$\Delta G_{Cr}^{E} = RTln\left(\frac{\gamma_{Cr}^{\varphi}\gamma_{Fe}^{B}}{\gamma_{Fe}^{\varphi}\gamma_{Cr}^{B}}\right) . \tag{6}$$

For a non-ideal solution, the excess Gibbs energy is not zero and shall not be ignored. The solid solution of Fcc(Fe) with dissolved Cr is a non-ideal solution. For a regular solid solution,

$$RTln\gamma_{Cr} = \overline{\Delta H_{Cr}} = \omega_{Fe\_Cr}(1-x_{Cr})^2 , \tag{7}$$

$$RTln\gamma_{Fe} = \overline{\Delta H_{Fe}} = \omega_{Fe\_Cr}(1-x_{Fe})^2 . \tag{8}$$

$\overline{\Delta H_{Cr}}$ and $\overline{\Delta H_{Fe}}$ are the partial mole enthalpy of Cr and Fe in Fcc(Fe,Cr), respectively. ω_{Fe_Cr} can be obtained from the recently assessed thermodynamics database [14]. Substituting Eqs. (7) and (8) into Eq. (6), the excess segregation energy can be described by

$$\Delta G_{Cr}^{E} = 2\omega_{FeCr}(x_{Cr}^{B} - x_{Cr}^{\varphi}) . \tag{9}$$

Then the total segregation energy is

$$\Delta G_{Cr} = \left(\mu_{Fe}^{B,0} - \mu_{Cr}^{B,0}\right) - \left(\mu_{Fe}^{\varphi,0} - \mu_{Cr}^{\varphi,0}\right) + 2\omega_{Fe\_Cr}(x_{Cr}^{B} - x_{Cr}^{\varphi}) . \tag{10}$$

Equation (10) suggests that the segregation energy of Cr in Fcc is highly dependent on the magnitude of ΔG_{Cr}^{0}, ω_{FeCr} and x_{Cr}^{φ}. Similarly, the segregation energy of Ni in Fcc is derived as

$$\Delta G_{Ni} = \left(\mu_{Fe}^{B,0} - \mu_{Ni}^{B,0}\right) - \left(\mu_{Fe}^{\varphi,0} - \mu_{Ni}^{\varphi,0}\right) + 2\omega_{Fe\_Ni}(x_{Ni}^{B} - x_{Ni}^{\varphi}) . \tag{11}$$

2.2 Kinetics model

The GB segregation kinetics is based on the Hofmann and Erlewein model [25], in which solute atoms move along a potential gradient with a direction perpendicular to the interface. The potential barrier is diffusion barrier ΔG_D in the bulk. The potential at GBs is lowered by the segregation energy ΔG_S, as shown in Fig. 1. To overcome difficulties with the solution of a diffusion equation in a potential gradient, this approach describes the attainment of concentration distributions by atomic fluxes based on reaction rate theory. This model assumes no concentration gradient occurring within atomic layers parallel to the GB plane, so that the model is confined to a one-dimensional problem.

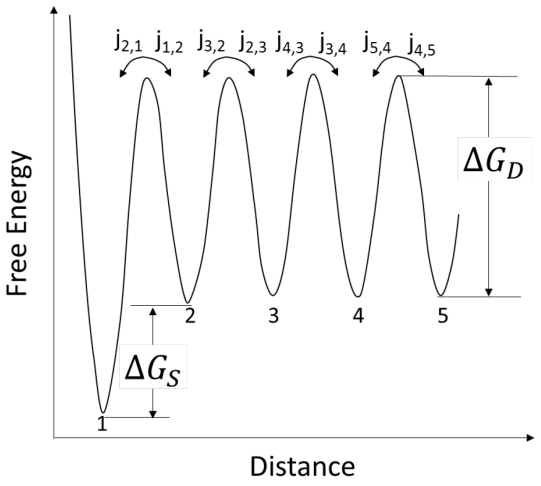

Figure 1. Assumed free energy versus depth for segregant atoms at the surface and in the bulk.

The GB segregation of solute Cr or Ni in Fcc(Fe) occurs as the solute atoms move along the potential gradient. The solute flux equations are described by Eqs. 12(a~d):

$$J_{12} = a_1^{-2} X_1 W_{12} \vartheta_1 \exp\left[-\frac{\Delta G_D - \Delta G_S}{RT}\right]. \quad (12a)$$

$$J_{21} = a_1^{-2} X_2 W_{21} \vartheta_2 \exp\left[-\frac{\Delta G_D}{RT}\right]. \quad (12b)$$

$$J_{23} = a_1^{-2} X_2 W_{23} \vartheta_2 \exp\left[-\frac{\Delta G_D}{RT}\right]. \quad (12c)$$

…

$$J_{i,i+1} = a_i^{-2} X_i W_{i,i+1} \vartheta_i \exp\left[-\frac{\Delta G_D}{RT}\right]. \quad (12d)$$

where a_i is the atomic jump distance, X_i is the concentration of solute atoms in layer "i", ϑ_i is the solute atom oscillation frequency, and $W_{i,i+1}$ is the jump probability factors of the solute atoms. In a first order approximation, all jump frequencies are assumed to be equal, as well as the jump distances. The deviation for a_1 and ϑ_1 from this assumption will be accounted for by segregation energy. In the kinetic modeling, the segregation energy ΔG_S for Cr and Ni in Fcc(Fe) will be derived in Section 3.1. The ΔG_D is the activation energy for diffusion through vacancy, it will be derived from the mobility database of Fe-Cr-Ni [14].The jump probability factor was assigned using the following relationship based on Hofmann's work:

$$w_{21} = X_S^M - X_S\,, \quad (13a)$$

$$W_{12} = 1 - X_2\,, \quad (13b)$$

$$W_{23} = 1 - X_3\,, \quad (13c)$$

$$W_{i,i+1} = 1 - X_{i+1}\,, \quad (13d)$$

where X_S is surface composition and X_S^M is the maximum allowable surface coverage. In this study, X_S^M equals 1.

Computational codes for calculating the thermodynamics and kinetics of thermal segregation were implemented using Matlab. The system was modeled by N parallel atomic planes perpendicular to the diffusion axis. The first plane corresponds to the GB plane and planes >1 get into the bulk. The maximum plane ends at about 1μm distance from GB. The flux is set to zero between plane <1 and Plane=1 or plane >max and plane=max. The ODE15 solver with variable time step algorithm in the Matlab was used to solve the differential equations. Note that the influence of defect sink characteristics such as GB structure is neglected in the following discussion; it is assumed that all sinks act according to perfect sink criteria and hence approximate RIS observed at random high-angle GBs. This approximation was used to simplify the presentation of the model and analysis.

3. Thermal segregation in Fe-Cr-Ni alloys

We systematically studied thermal segregation of a Fe-Cr-Ni alloy as a function of temperature and time, which is a component of an integrated frame work of TES-RIS modeling (Thermal equilibrium segregation-Radiation induced segregation). The first part of this work is to derive the standard molar Gibbs energy of segregation of Cr and Ni (ΔG_{Cr}^{0} and ΔG_{Ni}^{0}).

3.1 Derivation of segregation energy at standard state

Based on thermodynamics of surface and interface equilibrium, the partial interfacial energy of element *i* should be equal to that of element *j*:

$$\sigma_i^{\circ}\frac{\omega_i^{\circ}}{\omega_i}+\frac{RT}{\omega_i}\ln\left(\frac{x_i^{GB}}{x_i}\right)+\frac{\Delta_i^{E,GB}-\Delta_i^{E}}{\omega_i}=\sigma_j^{\circ}\frac{\omega_j^{\circ}}{\omega_j}+\frac{RT}{\omega_i}\ln\left(\frac{x_j^{GB}}{x_j}\right)+\frac{\Delta_j^{E,GB}-\Delta_j^{E}}{\omega_j} \qquad (14)$$

Assume all components have equal atomic sizes, i.e., the molar GB interfacial areas of all components are equal and not composition dependent ($\omega_i=\omega_j=\omega_i^{\circ}=\omega_j^{\circ}=\omega$), then

$$\frac{x_j^{GB}}{x_i^{GB}}=\frac{x_j}{x_j}\exp\left[\frac{\sigma_i^{\circ}\omega-\sigma_j^{\circ}\omega+(\Delta_i^{E,GB}-\Delta_i^{E})-(\Delta_j^{E,GB}-\Delta_j^{E})}{RT}\right] \qquad (15)$$

$$\Delta G_j^{\circ,seg}=\sigma_i^{\circ}\omega-\sigma_j^{\circ}\omega \qquad (16)$$

Assume *i* is Fe, and *j* is Cr and Ni. The average values of σ_{Ni}° is 0.85 ($\frac{J}{m^{-2}}$), then based on Nastar's work [26], $\sigma_{Cr}^{\circ}=0.91\sigma_{Ni}^{\circ}=0.93\sigma_{Fe}^{\circ}$, the average value of σ_{Cr}° and σ_{Fe}° is 0.7735 $\left(\frac{J}{m^2}\right)$ and 0.832 ($\frac{J}{m^2}$). The molar GB interfacial area can be calculated from the equation below:

$$\omega=fV^{\frac{2}{3}}N^{\frac{1}{3}} \qquad (17)$$

In which, N is Avogadro constant $6.022 \times 10^{23}(\frac{1}{mol})$, V is the molar volume $(\frac{m^3}{mol})$, and f is a dimensionless geometrical constant. For fcc structure, f is about 1.24. Based on the assessment in literature [27], the molar volume of Fcc(Fe) can be written as:

$$V(T) = V_0 \exp\left(\int_{T_0}^{T} 3\alpha dT\right) \quad (18)$$

where V_0 is the molar volume at the reference temperature, T_0. α denotes the coefficient of linear thermal expansion (CLE) of a phase in the nonmagnetic state.
For a cubic structure,

$$3\alpha = a + bT + cT^2 + dT^{-2} \quad (19)$$

For Fcc(Fe), $V_0 = 6.72092 \times 10^{-6}$ $(\frac{m^3}{mol})$, $a = 6.97895 \times 10^{-5}(K^{-1})$ and b, c and d are zero. This formula can be used to describe pure Fcc(Fe) at temperature over 298K. Combining Eq. (18) and (19), and plugging into V_0 and a, the molar volume of Fe_Fcc can be described as:

$$V(T) = 6.72092 \times 10^{-6} + 4.69 \times 10^{-10}T \quad (20)$$

Therefore, the segregation energy of Cr is

$$\Delta G_{Cr}^{\circ,seg} = 6021016(6.72092 \times 10^{-6} + 4.69 \times 10^{-10}T)^{\frac{2}{3}} \quad (21)$$

And that for Ni is

$$\Delta G_{Ni}^{\circ,seg} = -1989553(6.72092 \times 10^{-6} + 4.69 \times 10^{-10}T)^{\frac{2}{3}} \quad (22)$$

Based on Eq. (21) and (22), in the temperature range from 298K to 1498K, the value of $\Delta G_{Cr}^{\circ,seg}$ is in the range of 2173 to 2291J/mol, and that for $\Delta G_{Ni}^{\circ,seg}$ is -718 to -757J/mol. This suggests that thermal segregation will lead to enrichment of Cr and depletion of Ni at grain boundaries.

3.2 Calculated results on thermal equilibrium GB segregation of Cr and Ni

In this section, we show the simulation results on TES of Fe-19Cr-12Ni (at%) at different temperatures with different time periods. Figure 2 shows the composition of Cr and Ni at GBs in the temperature range from 350 to 1200°C. At all temperatures, the calculated results show the enrichment of Cr and depletion of Ni at GB. The two horizontal lines represent the bulk composition. The lines with symbols represent the calculated GB compositions. The magnitude of Cr enrichment is two to three times larger than that of Ni depletion. The magnitude of Cr enrichment or depletion of Ni decreases with increasing temperatures.

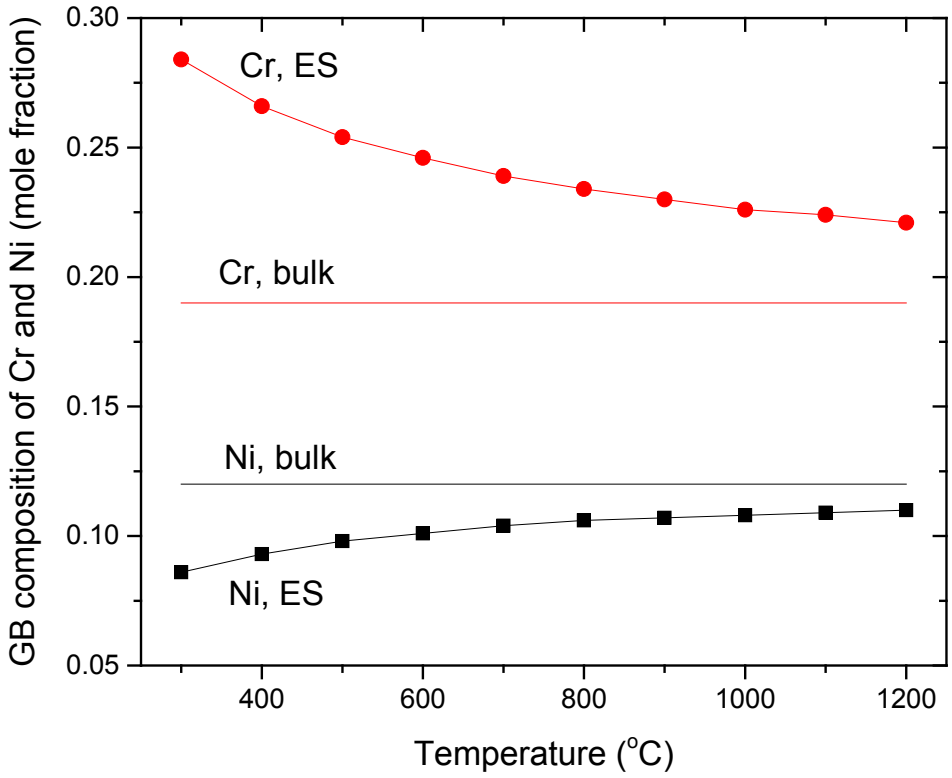

Figure 2 Cr and Ni segregation at grain boundary as a function of temperature

Isothermal segregation kinetics curves of Cr and Ni at different temperatures were plotted in Fig. 3. While the results in Fig. 2 tell the maximum allowable segregation under thermodynamic equilibrium, the results in Fig. 3 show how long it would take for the alloy to reach those values at different temperatures, i.e., the composition of Cr and Ni as a function of time. At each temperature, the segregation kinetics of Cr is represented by a "S" shape curve. Ni looks similar but in a depletion mode. This simulation results suggested at 1200°C, the equilibrium segregation level can be reached with 1e-8 hour, i.e., 3.6e-5 second. While in the LWRs operation temperature regime 300°C, the alloy will reach equilibrium segregation in about 10^8 hours, which is about 11384 years. This suggested segregation at 300°C will never reach thermal equilibrium under practical situations. However, we have seen routine reports about Cr enrichment in pre-irradiated samples. Apparently, that enrichment is not due to TES at 300°C, but a result of either segregation retained from high temperature or Thermal Non-Equilibrium-Segregation that formed during processing such as quenching.

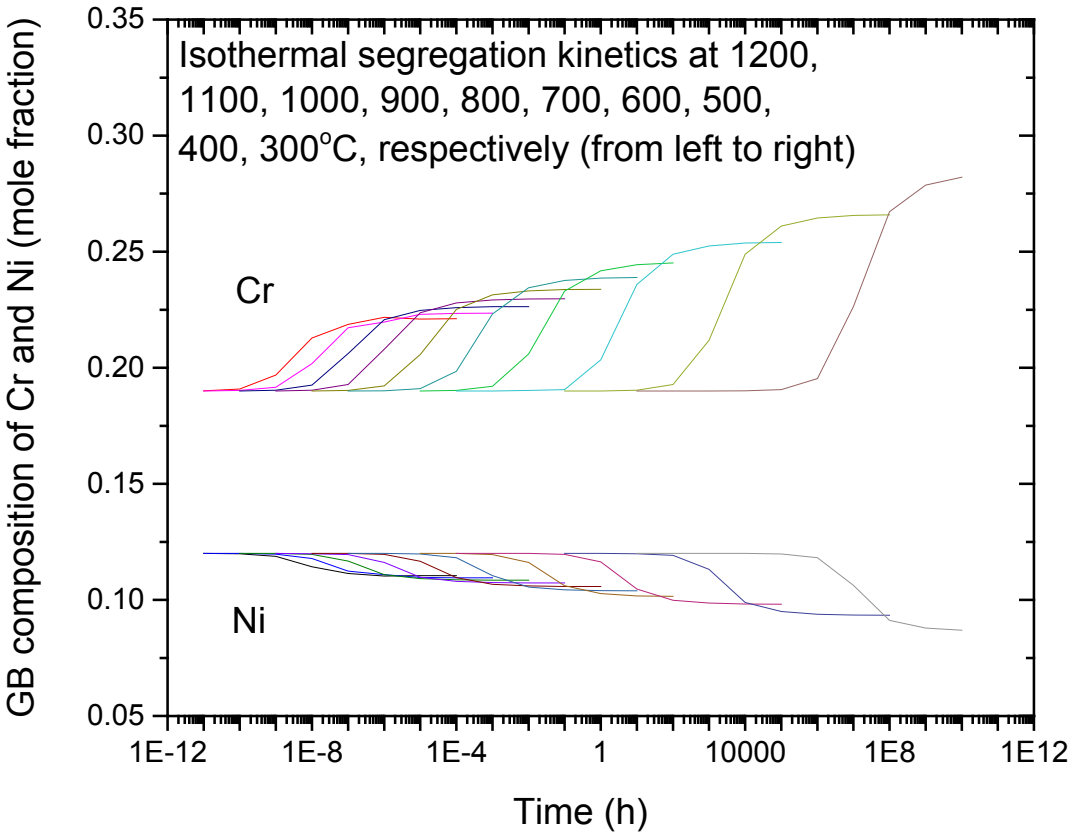

Figure 3 The isothermal segregation kinetics of Cr and Ni at temperatures of 1200, 1100, 1000, 900, 800, 800, 700, 600, 500, 400 and 300°C, represented by curves from left to right, respectively.

4. Integrated modeling on thermal equilibrium segregation and radiation induced segregation in Fe-Cr-Ni alloys

4.1 Integration strategy between TES and RIS modeling

Modeling on radiation-induced segregation (RIS) in Fe-Cr-Ni alloys has been described in detail previously [14], and will not be repeated here. To integrate the current TES modeling with the previous RIS modeling, we intentionally designed and developed the TES modeling with many common features as the RIS modeling, to facilitate the direct integration. These common features are: 1) the chemical potential of each element was calculated using the Gibbs energy functions stored in the same Fe-Cr-Ni thermodynamic database; 2) The diffusion coefficient of each element via vacancy was calculated from the same Fe-Cr-Ni mobility database. 3) The same kinetics modeling frame work was used, i.e., the system was modeled by N parallel atomic planes perpendicular to the diffusion axis and the potential barrier in the bulk is diffusion barrier ΔG_D. Besides these common features, several differences between RIS and TES need special attention during the integration process. First, the defect concentration in RIS is determined by dpa rate, irradiation time, defect combination and annihilation. The resulted defect concentration

usually is much higher than that under thermal condition, therefore, the diffusion is much enhanced. Second, the driving force for diffusion under simultaneous RIS and TES is the combination of chemical gradients of defects between bulk and GB, and the lower energy state at GBs reduced by the solute segregation energy. Third, the interstitial diffusion can be ignored in TES due to negligible interstitial concentration, but not in RIS. In this work, a general diffusion coefficient equation was used to accommodate both the radiation-induced defect concentration and thermal-induced defect concentration. For the boundary condition of the first plane at GBs, the changing rate of defect is kept as zero (perfect sink condition), and the flux of element Cr, Fe and Ni as zero. It should be emphasized that the diffusion flux for the first plane at GBs need to take the segregation energy into consideration. In the deep inside, the flux of all elements and defects were set to zero. The ODE15 solver with variable time step algorithm in the Matlab was used to solve the differential equations.

4.2 Simulation results from integrated modeling

We simulated and compared the GB segregation under different conditions with or without pre-existing segregation, as summarized in Table 1. The first set of simulations assumed no prior heat treatment, i.e., no pre-existing GB segregation. This set of simulations was performed under simultaneous thermal and radiation conditions (dpa rate is 8e-7dpa/s) for 1, 10, 100 and 1000 hours at 400°C. The second set of simulations assumed the pre-existing GB segregation resulted from thermal equilibrium annealing at 400°C. We used the same temperature as the subsequent irradiation temperature to generate similar comparison. Then we conducted the same integrated simulation for TES and RIS as those in the first set of simulations. The comparison of results from these two set of simulations can provide guidance on how

Table 1: Summary of simulation conditions

Simulation	1	2
Alloy buck composition	Alloy Composition: Fe-19Cr-12Ni (at%)	Alloy Composition: Fe-19Cr-12Ni (at%)
Prior heat treatment	No	Yes, annealed at 400C for 10000h to generate the equilibrium segregation
Pre-existing GB segregation	No	Yes, from prior heat treatment
Irradiation	Yes, at 400C for 1, 10, 100 and 1000h with dpa rate 8e-7 dpa/s	Yes, at 400C for 1, 10, 100 and 1000h with dpa rate 8e-7 dpa/s

The initial concentration profiles of Cr and Ni for simulations #1 and #2 before irradiation are shown in Fig. 4. The dashed lines denote simulation #1 which has no pre-existing GB segregation. The solid lines denote simulation #2 assuming the pre-existing GB segregation resulted from prior thermal equilibrium annealing at 400°C

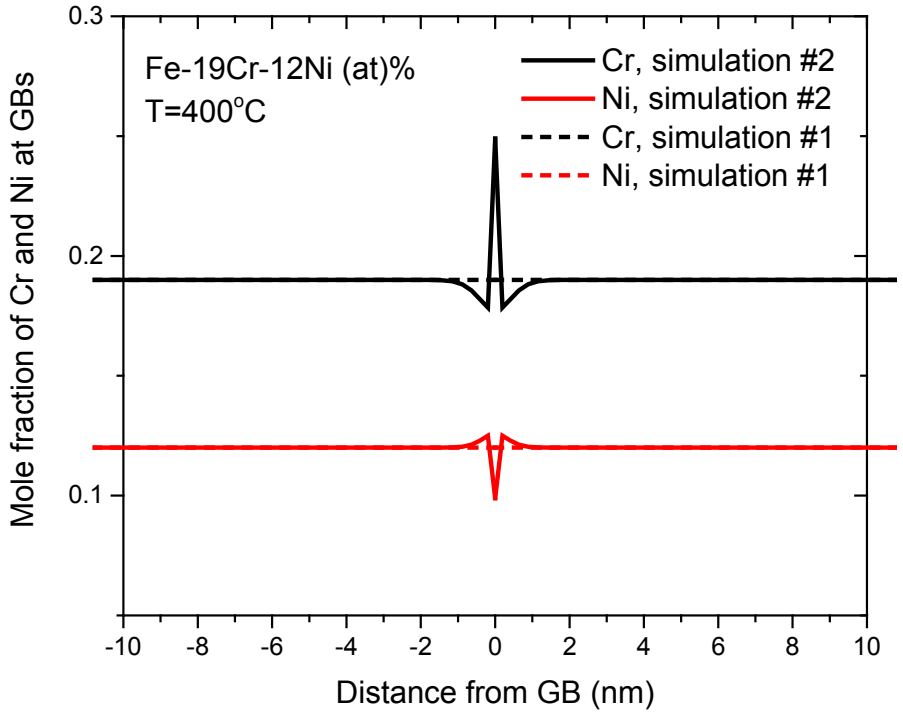

Figure 4 Initial concentration profiles of Cr and Ni for simulations #1 and #2 before irradiation starts.

The simulation results of Cr and Ni after irradiation for both cases with and without pre-existing are shown in Figs. 5 and 6, respectively. The segregation profiles of Cr and Ni in the GB region were plotted in different colors for 1, 10, 100 and 1000h, respectively. The solid lines denote simulation #1 assuming no pre-existing segregation at GB. The short-dashed lines with markers denote simulation #2 assuming pre-existing GB segregation. There are two findings through comparison:

1) The pre-existing GB segregation only affects the subsequent segregation in the short time. For example, pre-existing Cr enrichment leads to a less Cr depletion at 1h, and pre-existing Ni depletion leads to a less enrichment of Ni at 1h. However, at 10, 100, and 1000h, the difference in segregation profiles is negligible, as shown by the overlapping between the solid lines and dashed lines. These findings are consistent with Busby et al.'s [17] observation of the transitory w-shape profile.

2) For the same element, the segregation tendency due to TES is opposite to it from RIS. These opposite tendency leads to the formation of w-shape profile. While TES only affects the distance of one or two atomic layers from GB, the RIS can affect a broader distance from GB. Considering the measurement resolution of Auger of STEM analysis, the segregation tendency due to RIS may play a dominant role in the measured values. However, The GB segregation due to TES may affect the chemical potential of element at GB, and subsequently the corrosion resistance.

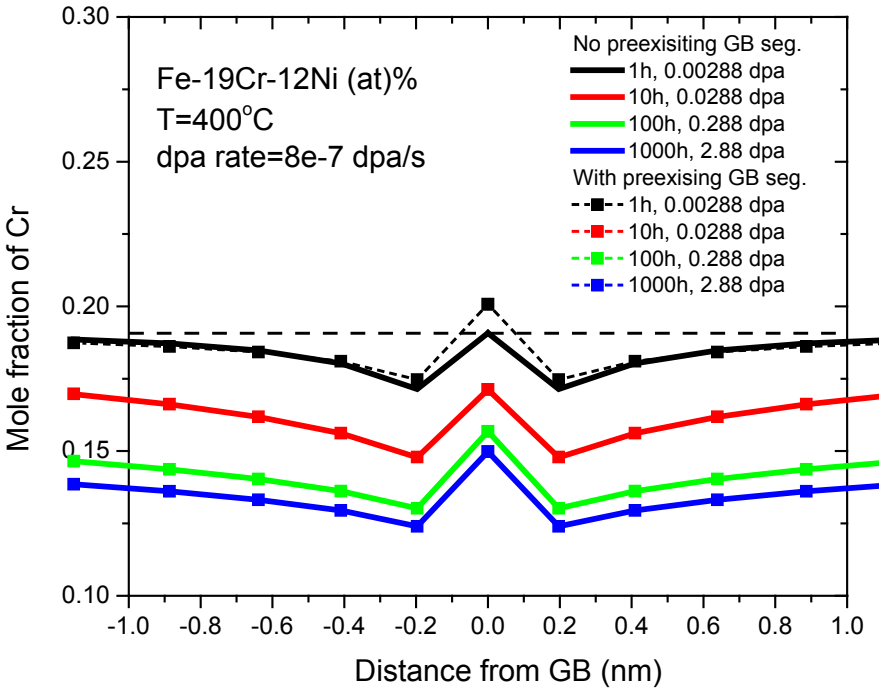

Figure 5 Comparison of segregation profile of Cr in the vicinity of GB with pre-existing GB segregation (short dashed lines) and without such segregation (solid lines)

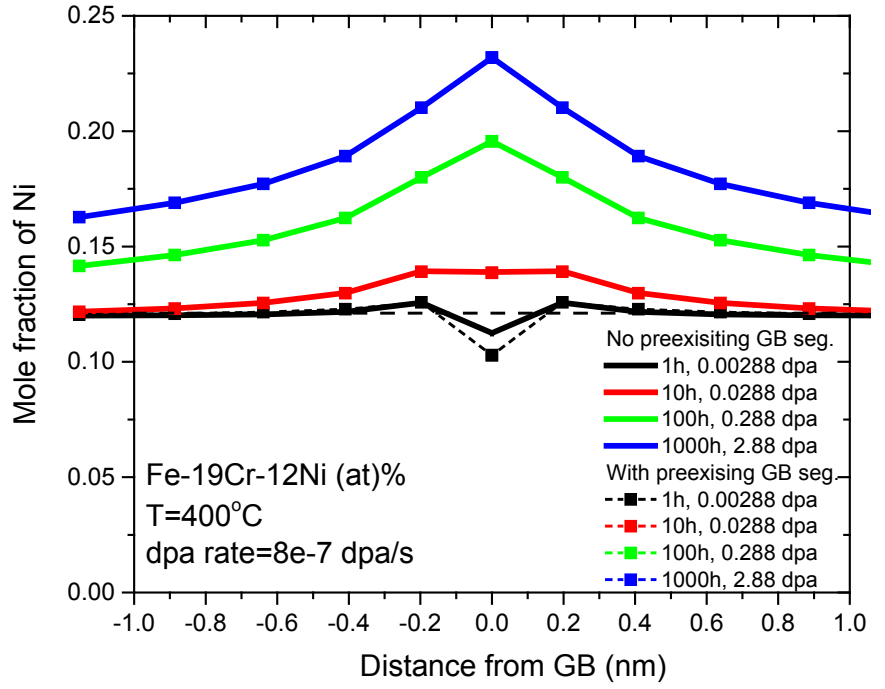

Figure 6 Comparison of segregation profile of Cr in the vicinity of GBs with pre-existing GN segregation (short dashed lines) and without such segregation (solid lines)

For the case with pre-exisiting GB segregation, we compared the concentration profile at 0 dpa (dashed line) and at 28.8 dpa (solid line) in Fig. 7. It clearly shows the concentration profiles at 28.8 dpa is dominated by the irradiation effect. Although the Cr concentration at the GB layer is enriched compared to the neighboring layer, it is depleted compared to the initial concentration or the concentration in the bulk. The "W-shape" in Cr profile formed due to pre-existing GB segregation is much narrower than that formed due to composition gradient from transient state as shown in previous work [14].

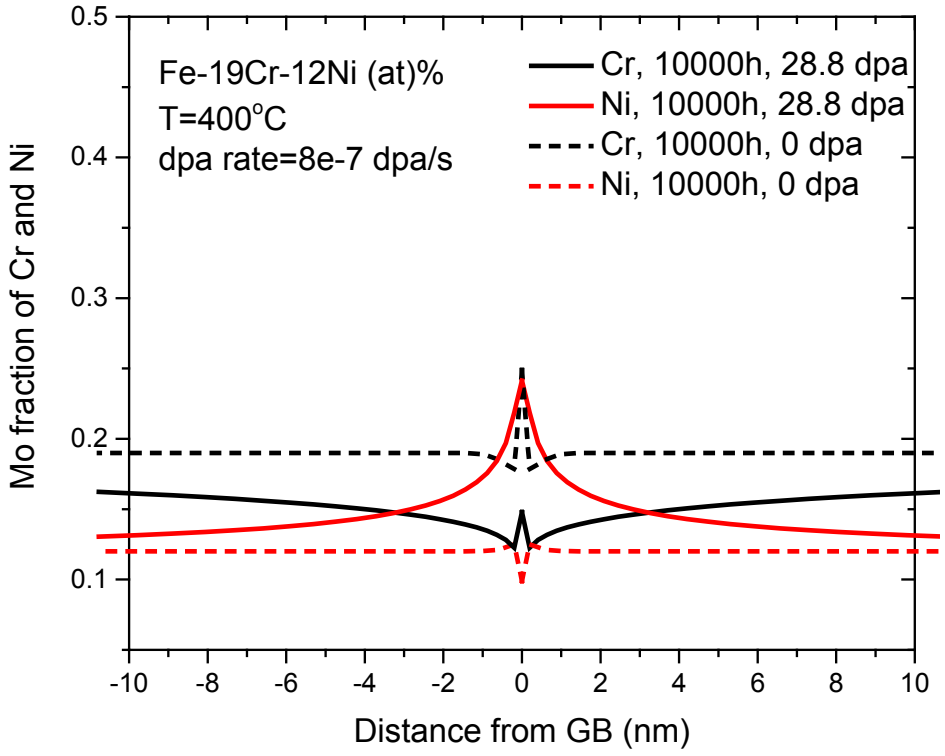

Figure 7 Comparison between the calculated concentration profiles of Cr and Ni at 0 dpa (dashed line) and those at 28.8 dpa (solid line).

5. Prediction on phase stability of $Ni_2(Cr,Mo)$ phase in Fe-Cr-Ni-Mo system

Thermodynamic models of phases in the Fe-Cr-Ni-Mo quaternary system have been developed in a prior work [28]. The intermetallic phases modeled in previous work were mainly the high temperature phases such as Chi-phase, Laves-phase and Sigma phase. The $Ni_2(Cr,Mo)$ phase is stable at low temperature regime (<700°C). The ordering of $Ni_2(Cr,Mo)$ is similar to Pt_2Mo-type (oP6 or C11b), which is a superstructure of the Fcc structure. Turchi et al.[29], has thermodynamically modeled this phase in the Cr-Mo-Ni-W system, in which the Ni2(Cr,Mo)

phase was modeled by a two-sublattice model (Cr, Mo,W)$_1$(Mo,Ni,W)$_2$. This model was adopted in the current modeling of Ni_2(Cr,Mo) phase in the Fe-Cr-Ni-Mo system. W was taken away from the model. The Fe was introduced into the second sublattice to demonstrate its substitution with Ni. Therefore, the model used in this work is (Cr,Mo)$_1$(Fe,Mo,Ni)$_2$. The Gibbs energy of the Ni_2(Cr,Mo) was described by Compound Energy Formalism (CEF) [30]. The formalism is described as below:

$$G_m^{\varphi} = \sum_i y_i^I y_j^{II} G_{i:j}^{\varphi,\circ} + RT(\sum_i y_i^I \ln(y_i^I) + 2 * \sum_j y_j^{II} ln(y_j^{II})) + G_m^{\varphi,ex}(y) \quad (23)$$

Optimized thermodynamic model parameters for the Ni_2(Cr,Mo) phases in the Fe-Cr-Mo-Ni system are listed below. (Other model parameters are available from literature [31]). The temperature range of the parameters is between 298.15 and 6000 K unless otherwise denoted. Unit is J/(mol. formula). $G_{Cr}^{bcc,0}$, $G_{Fe}^{bcc,0}$, $G_{Ni}^{fcc,0}$, and $G_{Mo}^{bcc,0}$ are taken from the SGTE pure element database [32].

Ni2Cr : (Cr,Mo)$_1$(Fe,Mo,Ni)$_2$

$$L_{Cr:Ni}^0 = G_{Cr}^{bcc,0} + 2 * G_{Ni}^{fcc,0} - 7095 - 5.6 \times T$$
$$L_{Mo:Ni}^0 = G_{Mo}^{bcc,0} + 2 * G_{Ni}^{fcc,0} - 5000$$
$$L_{Cr:Mo}^0 = G_{Cr}^{bcc,0} + 2 * G_{Mo}^{bcc,0} + 350000$$
$$L_{Mo:Mo}^0 = 3 * G_{Mo}^{bcc,0} + 35000$$
$$L_{Cr:Mo,Ni}^0 = -12250$$
$$L_{Cr:Fe}^0 = G_{Cr}^{bcc,0} + 2 * G_{Fe}^{bcc,0} + 5000$$

The validation of thermodynamic modeling was performed through the comparison between the calculated binary/ternary phase diagram and the literature information, which is not shown here. The calculated results for the multicomponent system was compared with long-term thermal aging data of C22 at 610°C. The experimental data from high temperature aging is from the Gary Was Group at UM. In this aged C22 alloy, the Ni_2(Cr,Mo) phase was formed and the compositions of the matrix and Ni_2(Cr,Mo) phase were measured through Atom Probe Tomography. The calculated phases and amount of each phase of the C22 alloy was plotted as a function of temperature in Fig. 8. It shows the formation temperature of Ni_2(Cr,Mo)is around 640°C, slightly higher than the annealing temperature. In addition to the Ni_2(Cr,Mo) phase, it also forms the P phase, another intermetallic phase. Although the P phase was not subjected to careful characterization, the calculation results are consistent with the observation of some grain boundary precipitates in this alloy. The comparison between the calculated and APT measured compositions for the Matrix and Ni_2(Cr,Mo) precipitates is shown in Fig. 9 (a) and (b), respectively.

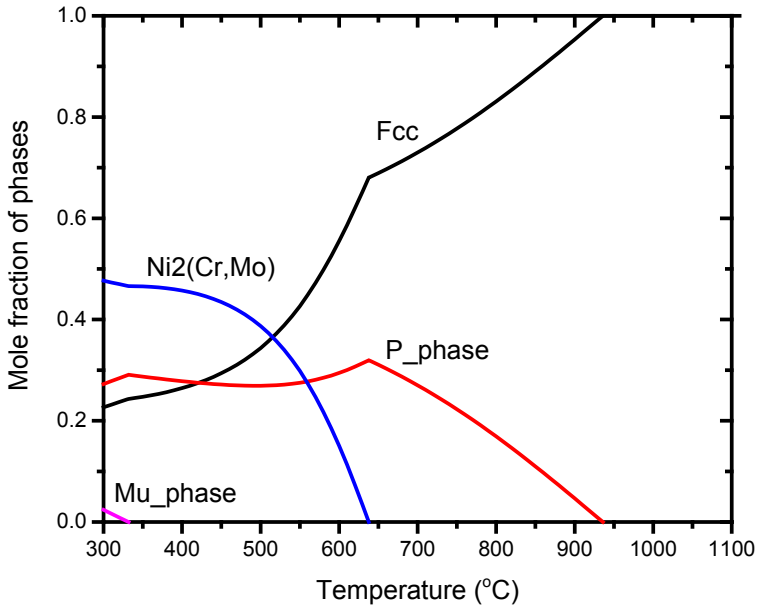

Figure 8 Calculated mole fraction of phases in the C22 alloy as a function of temperature

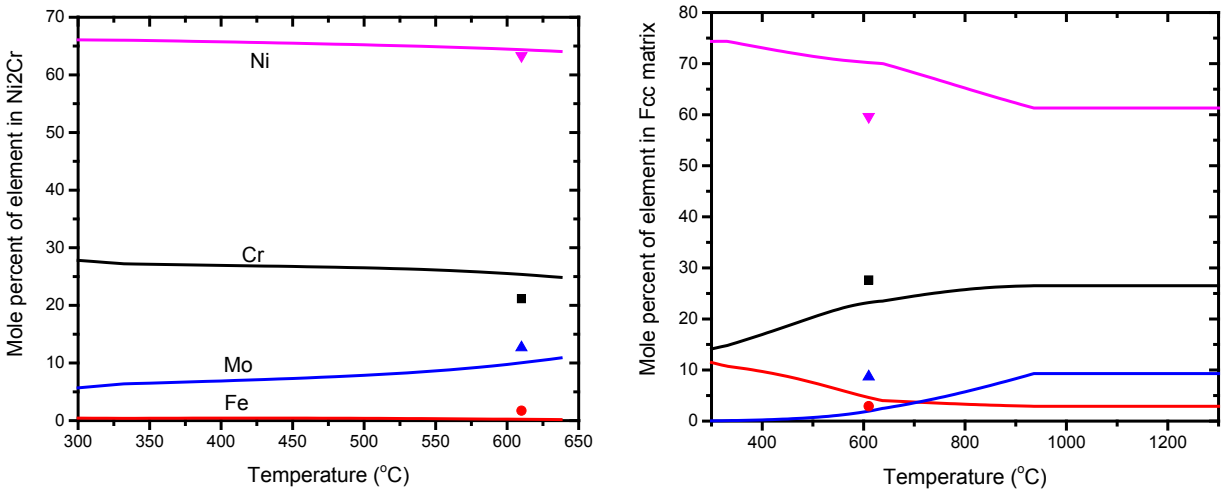

Figure 9 Comparison between the calculated phase compositions and experimental measurement at 610°C (a) for the $Ni_2(Cr,Mo)$ and (b) for the matrix

Once the thermodynamic models of the Fe-Cr-Ni-Mo system has been validated, we used it to predict the equilibrium amount of $Ni_2(Cr,Mo)$ in the selected Ni-based alloys at 360°C (i.e., 625, 625Plus, 625DA, 725, X750, 718A, 690, and C22), and then compare the calculated results with those observed in irradiated materials (again the experimental data is from the Gary Was Group at UM). The composition of Fe, Cr, Ni and Mo in these alloys are listed in Table 2, which were normalized into 100%. The calculated $Ni_2(Cr,Mo)$ amount in mole percent as a function Fe content the bulk alloy is shown in Fig. 10 (a), and the observed $Ni_2(Cr,Mo)$ amount in volume percent is in Fig. 10 (b). The comparison shows the calculated and experimental results following the same trend. For the alloy that has the lowest Fe, the amount of $Ni_2(Cr,Mo)$ is the greatest. For alloy with higher Fe such as 718 and 706, there is no $Ni_2(Cr,Mo)$. It should be noted

that the calculated absolute values are higher than the experimental ones. A small part of the discrepancy may come from the density difference of different phases; therefore the mole percent is not 1:1 ratio to the volume percent. The consistently higher amount in calculation suggested the observed $Ni_2(Cr,Mo)$ may not reach equilibrium value yet. The amount of $Ni_2(Cr,Mo)$ is likely to increase more with further irradiation. The thermodynamic stability analysis suggested that while 360°C is too low to allow reasonable diffusion under thermal condition, the formation of $Ni_2(Cr,Mo)$ is feasible in irradiation materials due to radiation enhanced diffusion.

Table 2 The compositions of Fe, Cr, Ni and Mo in selected Ni alloys

Alloy	Ni at%	Cr at%	Mo at%	Fe at%
625	64.00	26.50	5.63	3.87
625DA	65.66	24.65	5.40	4.29
625plus	63.52	22.08	8.44	5.96
725	60.52	25.52	5.19	8.77
690	57.34	32.111	0.006	10.543
C22	61.27	26.49	9.28	2.96
706	39.26	17.78	41.13	1.84
718	55.37	21.86	1.86	20.90

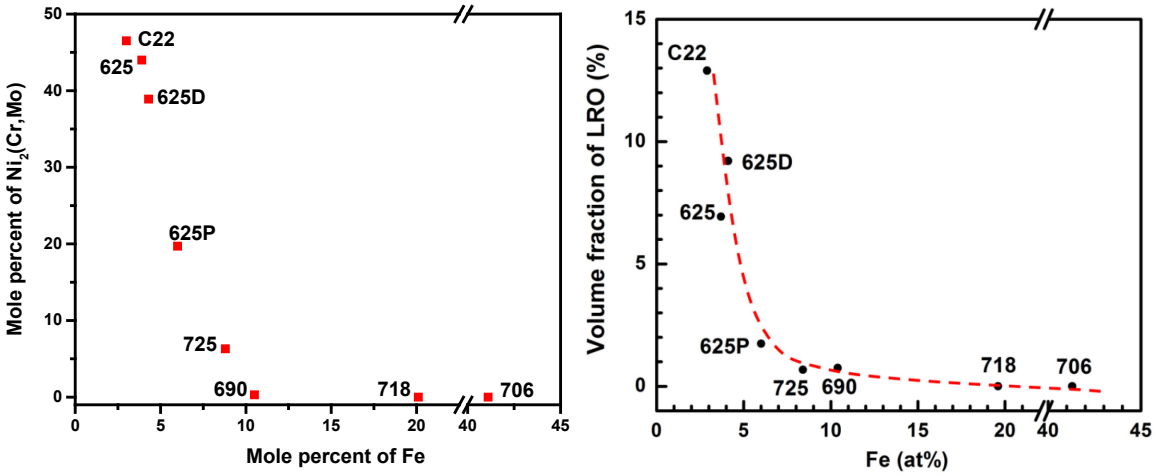

Figure 10 Comparison between the calculated amount of Ni2(Cr,Mo) under (a) equilibrium thermal condition and (b) irradiation condition.

6. Summary of conclusions

This work aims at developing computational tools for modeling thermal and radiation effects on solute segregation at grain boundaries, and thermodynamic stability of Ni2(Cr,Mo) phase in Fe-Cr-Ni-Mo system. The major outcomes from this work are listed in the following:

1) Under the simultaneous thermal and irradiation conditions, radiation-induced segregation played a dominant role in the GB segregation. The pre-existing GB segregation only affects the subsequent radiation-induced segregation in the short time. For the same element, the segregation tendency of Cr and Ni due to TES is opposite to that from RIS. These opposite tendency leads to the formation of w-shape profile. These findings are consistent with Busby et al.'s [17] observation of the transitory w-shape profile.
2) While TES only affects the distance of one or two atomic layers from GB, the RIS can affect a broader distance from GB. Therefore, the W-shape due to pre-existing GB segregation is much narrower than that due to composition gradient formed during transient state. Considering the measurement resolution of Auger of STEM analysis, the segregation tendency due to RIS should play a dominant role in the measured values. However, The GB segregation due to pre-existing GB segregation may affect the chemical potential of element at GB, and subsequently the corrosion resistance.
3) Based on the newly developed thermodynamic database of Fe-Cr-Ni-Mo, we predicted the $Ni_2(Cr,Mo)$ as a thermodynamically stable phase in all investigated low Fe-content Ni-alloys. The calculated phase amount decreases with the increasing Fe content, being consistent with that observed in the irradiated materials.
4) The formation of the $Ni_2(Cr,Mo)$ phase in irradiated materials is due to irradiation enhanced diffusion. The calculated equilibrium $Ni_2(Cr,Mo)$ amount is more than that observed in the irradiated materials, suggesting that the amount of $Ni_2(Cr,Mo)$ is likely to increase more with further irradiation.

7. Future work

The following work is planned in the next step:

1) Continue the development of thermodynamic modeling tools on phase stability and solute segregation in irradiated materials.
2) Extend the modeling tools into multicomponent alloys with more elements such as Mo, Ti, Si.

8. References

1. Allen, T. and J. Busby, *Radiation damage concerns for extended light water reactor service.* JOM, 2009. **61**(7): p. 29-34.
2. Fukuya, K., *Current understanding of radiation-induced degradation in light water reactor structural materials.* Journal of Nuclear Science and Technology, 2013. **50**(3): p. 213-254.
3. Garner, F., *4.02-Radiation Damage in Austenitic Steels,"*. 2012, Oxford: Elsevier. p. 33-95.
4. Kenik, E.A. and J.T. Busby, *Radiation-induced degradation of stainless steel light water reactor internals.* Materials Science and Engineering: R: Reports, 2012. **73**(7): p. 67-83.
5. Zinkle, S.J. and G. Was, *Materials challenges in nuclear energy.* Acta Materialia, 2013. **61**(3): p. 735-758.
6. Allen, T.R. and G. Was, *Modeling radiation-induced segregation in austenitic Fe–Cr–Ni alloys.* Acta materialia, 1998. **46**(10): p. 3679-3691.
7. Field, K.G., et al., *Defect sink characteristics of specific grain boundary types in 304 stainless steels under high dose neutron environments.* Acta Materialia, 2015. **89**: p. 438-449.
8. Hashimoto, T., Y. Isobe, and N. Shigenaka, *A model for radiation-induced segregation in fcc binary alloys.* Journal of nuclear materials, 1995. **225**: p. 108-116.
9. Lam, N., *Compositional changes in Fe-Cr-Ni alloys under proton bombardment at elevated temperatures.* Journal of Nuclear Materials, 1983. **117**: p. 106-112.
10. Marwick, A., *Segregation in irradiated alloys: the inverse Kirkendall effect and the effect of constitution on void swelling.* Journal of Physics F: Metal Physics, 1978. **8**(9): p. 1849.
11. Takahashi, H. and N. Hashimoto, *Radiation-induced segregation and grain boundary migration in Fe–Cr–Ni model alloy under irradiation.* Materials Transactions, JIM, 1993. **34**(11): p. 1027-1030.
12. Watanabe, S., et al., *Quantitative studies of irradiation-induced segregation and grain boundary migration in Fe Cr Ni alloy.* Journal of nuclear materials, 1995. **224**(2): p. 158-168.
13. Wiedersich, H., P. Okamoto, and N.Q. Lam, *A theory of radiation-induced segregation in concentrated alloys.* Journal of Nuclear Materials, 1979. **83**(1): p. 98-108.
14. Yang, Y., et al., *Roles of vacancy/interstitial diffusion and segregation in the microchemistry at grain boundaries of irradiated Fe–Cr–Ni alloys.* Journal of Nuclear Materials, 2016. **473**: p. 35-53.
15. Perks, J., A. Marwick, and C. English, *A computer code to calculate radiation-induced segregation in concentrated ternary alloys.* 1986.
16. Lukas, H.L., S.G. Fries, and B. Sundman, *Computational thermodynamics: the Calphad method*. Vol. 131. 2007: Cambridge university press Cambridge.
17. Busby, J., et al. *Influence of initial grain boundary composition on the evolution of radiation-induced segregation profiles*. in *MRS Proceedings*. 1998. Cambridge Univ Press.
18. Cole, J.I., et al. *The Influence of Pre-Irradiation Heat Treatments on Thermal Non-Equilibrium and Radiation-Induced Segregation Behavior in Model Austenitic Stainless Steel Alloys*. in *Effects of Radiation on Materials: 21st International Symposium*. 2004. ASTM International.
19. Nastar, M. and F. Soisson. *Radiation-induced segregation*. 2012. Elsevier B.V.
20. EPRI, *Critical Issues Report and Roadmap for the Advanced Radiation-Resistant Materials Program*. 2012, EPRI: Palo Alto, CA and the U.S. Department of Energy, Washington, DC.
21. Hondros, E., et al., *Physical metallurgy, vol. 2North Holland*. 1996, Amsterdam.
22. MacLean, D., *Grain boundaries in metals.* 1957.
23. Lejcek, P., *Grain boundary segregation in metals*. Vol. 136. 2010: Springer Science & Business Media.
24. Du Plessis, J. and G. Van Wyk, *A model for surface segregation in multicomponent alloys—part I: Equilibrium segregation.* Journal of Physics and Chemistry of Solids, 1988. **49**(12): p. 1441-1450.

25. Hofmann, S. and J. Erlewein, *A model of the kinetics and equilibria of surface segregation in the monolayer regime.* Surface Science, 1978. **77**(3): p. 591-602.
26. Nastar*, M., *Segregation at grain boundaries: from equilibrium to irradiation induced steady states.* Philosophical Magazine, 2005. **85**(4-7): p. 641-647.
27. Lu, X.-G., M. Selleby, and B. Sundman, *Assessments of molar volume and thermal expansion for selected bcc, fcc and hcp metallic elements.* Calphad, 2005. **29**(1): p. 68-89.
28. Yang, Y., L. Tan, and J.T. Busby, *Thermal stability of intermetallic phases in Fe-rich Fe-Cr-Ni-Mo alloys.* Metallurgical and Materials Transactions A, 2015. **46**(9): p. 3900-3908.
29. Turchi, P.E., L. Kaufman, and Z.-K. Liu, *Modeling of Ni–Cr–Mo based alloys: Part I—phase stability.* Calphad, 2006. **30**(1): p. 70-87.
30. Hillert, M., *The compound energy formalism.* Journal of Alloys and Compounds, 2001. **320**(2): p. 161-176.
31. Yang, Y. and J. Busby, *Thermodynamic modeling and kinetics simulation of precipitate phases in AISI 316 stainless steels.* Journal of Nuclear Materials, 2014. **448**(1): p. 282-293.
32. Dinsdale, A.T., *SGTE data for pure elements.* Calphad, 1991. **15**(4): p. 317-425.